


Article

Reduction of spatially structured errors in wide-swath altimetric satellite data using data assimilation

Sammy Metref ^{1,*} , Emmanuel Cosme ¹, Julien Le Sommer ¹, Nora Poel ^{1,2}, Jean-Michel Brankart ¹, Jacques Verron ^{1,3} and Laura Gómez Navarro ^{1,4}

¹ Université Grenoble Alpes, CNRS, IRD, IGE, Grenoble, France.

² University of Potsdam, Institute for Computer Science, Potsdam, Germany.

³ Ocean Next, Grenoble, France.

⁴ Mediterranean Institute for Advanced Studies (IMEDEA) (UIB-CSIC), Esporles, Spain.

* Correspondence: sammy.metref@univ-grenoble-alpes.fr

Version April 29, 2019 submitted to Remote Sens.

Abstract: The Surface Water and Ocean Topography (SWOT) mission is a next generation satellite mission expected to provide a 2km-resolution observation of the sea surface height (SSH) on a two-dimensional swath. Processing SWOT data will be challenging, because of the large amount of data, the mismatch between high spatial resolution and low temporal resolution, and the observation errors. The present paper focuses on the reduction of the spatially structured errors of SWOT SSH data. It investigates a new error reduction method and assesses its performance in an observing system simulation experiment. The proposed error reduction method first projects the SWOT SSH onto a subspace spanned by the SWOT spatially structured errors. This projection is removed from the SWOT SSH to obtain a detrended SSH. The detrended SSH is then processed within an ensemble data assimilation analysis to retrieve a full SSH field. In the latter step, the detrending is applied to both the SWOT data and an ensemble of model-simulated SSH fields. Numerical experiments are performed with synthetic SWOT observations and an ensemble from a North Atlantic, 1/60° simulation of the ocean circulation (NATL60). The data assimilation analysis is carried out with an ensemble Kalman filter. The results are assessed with root mean square errors, power spectrum density and spatial coherence. They show that a significant part of the large scale SWOT errors is reduced. The filter analysis also reduces the small scale errors and allows to accurately recover the energy of the signal down to 25 km scales. In addition, using the SWOT nadir data to adjust the SSH detrending further reduces the errors.

Keywords: SWOT; correlated errors; OSSE; projection; detrending; ensemble Kalman filter

1. Introduction

The two-dimensional high resolution Surface Water Ocean Topography (SWOT) data have the potential to provide dense and accurate information on the dynamic of the meso- and submesoscale [12,16,17]. The considerable contribution of this unprecedented altimetric data for oceanography lays on two main characteristics of the SWOT data: (i) the two-dimensionality of the wide-swath data will provide a new insight on the ocean surface dynamic where the evolution of structures can be tracked and studied and (ii) the high resolution of the Ka-Band Radar Interferometer (KaRIn) instrument will allow to reach very fine scale structures (down to 15-km wavelength expected). However, the combination of these two SWOT characteristics inevitably leads to new challenges in the processing and treatment of the data.

The SWOT satellite and instrument design induces a string of cumulative, spatially structured errors, expected to have significant amplitudes in comparison with the signal, and to display strong

32 spatial correlations. The spatially structured errors will certainly induce strong limitations in the use of
33 SWOT data, and must be removed or at least reduced. Past works have addressed the reduction of the
34 small-scale, spatially uncorrelated noise [8,20] and the inclusion of the SWOT error correlations in data
35 assimilation [35,38]. Some techniques to correct the SWOT data long range correlated errors have been
36 investigated by Dibarboure and Ubelmann [10]. These techniques are based on the cross-calibration of
37 the satellite signal between multiple local zones in the satellite ground track. Information accumulated
38 over a certain period is used to retrieve the SWOT signal free of error. Although these techniques have
39 shown promising results, they only gain in accuracy as long as the ocean state remains relatively static
40 which is a strong hypothesis, especially for the temporal/spatial scale ratio of SWOT. An asset of the
41 error reduction method proposed in the present paper is that the SWOT signal is retrieved on each
42 pass of the satellite independently. In the future, the benefits of comparing the different approaches
43 could be explored.

44 In this paper, a new spatially structured error reduction method is presented which is composed
45 of two steps. The first step (detrending) removes from the data the across-track trends that may be due
46 to the spatially structured errors. Indeed, most of the expected SWOT errors have been intensively
47 investigated and are presented in an error budget [13]. This error budget shows that the errors will
48 strongly impact the spatial structure of the signal, especially across track, and are expected to create
49 artificially structured trends. This first step removes these trends which include the large scale errors
50 as well as a part of the large scale SWOT physical signal. The second step of the error reduction
51 method (retrieval) implements an ensemble data assimilation (DA) analysis to retrieve the large scale
52 physical signal. This ensemble DA analysis uses an ensemble of static high-resolution SSH scenes. As
53 an extension of the method, we also propose to further adjust the detrending with the SWOT nadir
54 data but in a rather simplistic way since the primary focus of this paper is the wide-swath data. Note
55 also that the method only deals, by construction, with the across-track structured errors of larger
56 scales. Hence, the method is not expected to reduce the two-dimensional structured errors (e.g. the
57 wet-troposphere error) and only partly reduce the uncorrelated errors (e.g. the KaRIn error). To reduce
58 the impact of these smaller scale errors, further developments of the method and/or combination with
59 other methods (e.g. [35,38]) will be needed.

60 The error reduction method is tested in the framework of an observing system simulation
61 experiment (OSSE). This framework, also known as twin experiments, consists in creating all the
62 data of the experiment – including the observations – from a simulation produced by a numerical
63 model and considered as the true ocean. Here, we use the high-resolution NATL60 (North Atlantic,
64 $1/60^\circ$ resolution) configuration [1,15] of the NEMO (Nucleus for European Modelling of the Ocean)
65 modelling system [29]. This simulation is one of the most advanced and high resolution simulation
66 available to this day, with an effective resolution of approximately 7km which is beneath the expected
67 effective resolution of the SWOT satellite. Note, however, that internal tides are not represented
68 in that simulation although studies have shown that internal tides should strongly impact the SSH
69 SWOT signal [22,34]. Internal tides should be included in future studies on this error reduction
70 method. In this study, we focus on the OSMOSIS region where the small scale structures are dominant
71 over the larger scales [6]. To create the observations from the NATL60 simulation we use the SWOT
72 simulator, a simulator of the ocean SWOT data, developed to help the scientific community prepare
73 the SWOT mission [18]. The SWOT simulator models six of the errors described in [13]: Ka-Band
74 Radar Interferometer (KaRIn) error, residual roll error, phase error, baseline dilatation error, timing
75 error and wet-troposphere error. Although not complete, these modelled errors are, to this day, the
76 best implemented prediction of what the largest SWOT errors will be.

77 The outline of the paper is the following: Section 2.1 describes the synthetic SWOT data created
78 by the SWOT simulator and used in the numerical experiments, the SWOT errors, and the error
79 reduction method. The overall target in the numerical experiments, presented in Section 3, is to
80 retrieve an error free SWOT observation. In this section, we assess (i) the benefit of using the detrended
81 SWOT data rather than the raw SWOT data in the error reduction method, (ii) the gain brought by

82 the detrended SWOT error reduction method over a standard Gaussian denoising filter and (iii) the
 83 potential of combining the SWOT data with its nadir altimeter data. A discussion is held in Section 4
 84 and conclusions are drawn in Section 5.

85

Science Orbit	
Repeat Cycle (days)	20.8646
Repeat Cycle (Orbits)	292
Sub-cycles (days)	1.10
Inclination	77.6
Elevation (km)	891

Table 1. Orbital characteristics of the Science Orbit implemented in the SWOT simulator and used in the present experiments.

86

87 2. Materials and Methods

88 2.1. Synthetic SWOT data

89 2.1.1. Synthetic SWOT data creation

90 The present study is conducted on an observing system simulation experiment (OSSE) which
 91 considers a high resolution model simulation to be the true state of the ocean. The simulation has been
 92 carried out with the NATL60 (North Atlantic, $1/60^\circ$ resolution) configuration of the NEMO (Nucleus
 93 for European Modelling of the Ocean) modelling system [29]. The horizontal resolution of $1/60^\circ$
 94 corresponds to 0.8 to 1.6 km, depending on latitude, while the vertical grid uses 300 levels. With this
 95 resolution, we can produce synthetic SWOT data that effectively observe the meso and submesoscale
 96 ocean circulation. The NATL60 simulation is the reference simulation in several studies [1,15]. More
 97 information on the model set up may be found on [31].

98 The region of study is the OSMOSIS region in the North Atlantic (44.821°N – 55.363°N ,
 99 20.016°W – 10.008°W ; [6]). The OSMOSIS region has very little large scale energy in comparison
 100 to the Gulf Stream [6]. This makes OSMOSIS an appropriate region for assessing the SWOT ability to
 101 recover small scale dynamics without having large scale structures strongly impact the diagnosis.

102 Synthetic SWOT data are created from NATL60-simulated SSH fields, using the SWOT simulator
 103 for Ocean Science [18,37] developed by the NASA Jet Propulsion Laboratory. In a first step, the SWOT
 104 simulator generates a data grid following the predefined swath geometry and orbit ground track.
 105 The characteristics of the simulated orbit are detailed in Table 1. The SWOT swath is 120 km wide
 106 with a 20 km gap in its center (Figure 1). The spatial resolution is 2km across and along track which
 107 leads to 50 grid points across track. The grid includes a nadir, along-track line with a resolution of 7
 108 km to simulate the nadir altimeter on board SWOT satellite. In a second step, the SWOT simulator
 109 interpolates the SSH input fields onto the SWOT grid (wide-swath and nadir). In a third and last step,
 110 the simulator randomly generates the main expected SWOT errors, following the specifications of the
 111 SWOT error budget document [13]. This is described in more details in the next subsection.

112 2.1.2. SWOT data errors

113 The SWOT simulator provides statistical models for six components of SWOT measurement
 114 errors [13,18]:

- 115 • Ka-Band Radar Interferometer (KaRIn) error

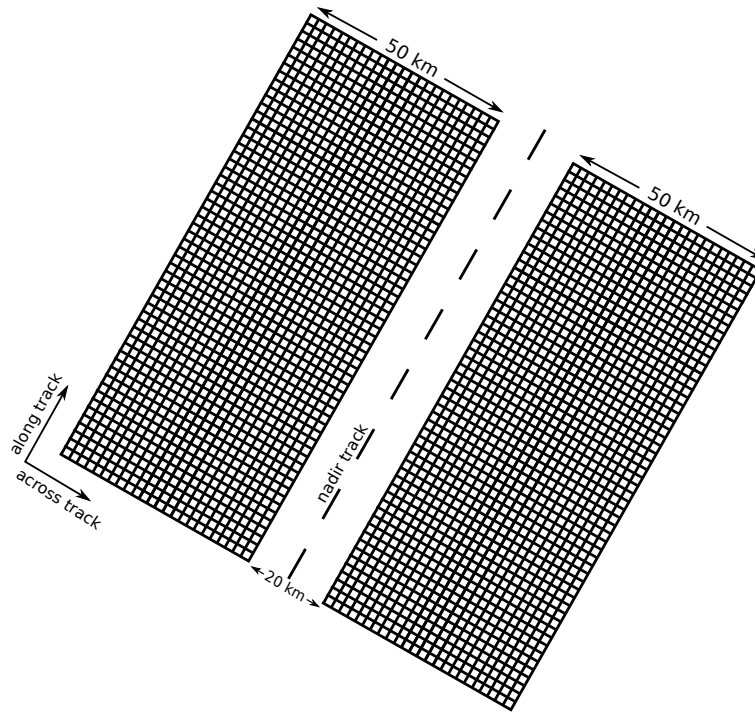


Figure 1. Schematic representation of the SWOT grid at 2 km resolution.

- 116 ● residual roll error
- 117 ● phase error
- 118 ● baseline dilatation
- 119 ● timing error
- 120 ● wet-troposphere error

121 The KaRIn instrument random error is a spatially uncorrelated noise with a non-constant variance
 122 across track (smiley curve). Several techniques have been developed to specifically denoise the KaRIn
 123 noise impacting the SWOT data [20,21]. In the present study, we focus on the spatially correlated
 124 errors. But we make the case that because DA is designed to deal with spatially uncorrelated noises,
 125 the KaRIn noise is expected to be also reduced by the DA analysis.

126 The spatially correlated errors have specific across track structures. Here, we only focus on the
 127 across track structure of the errors and we consider the error variation for all along track points x_a
 128 independently. A discussion on the implications of relaxing this assumption is proposed in Section 4.
 129 A schematic representation of the errors cross-track characteristics is presented in Figure 2.

The timing error directly impacts the height measurement and is due to a timing drift in the instrument signal propagation. It also depends on the look angle of the instrument but, at first order, this dependency can be neglected. The timing error e_0 is assumed to be constant across track:

$$e_0 = \alpha_0(x_a) \quad (1)$$

The roll error is due to the unknown interferometric roll angle, and increases linearly across the swath with the distance to the nadir point, i.e., the center of the swath ($x_c = 0$). The magnitude of this error can be large. For instance, a tilt of $1/10000^\circ$ generates a 6 cm error at a point 35 km away from the nadir point. The roll error is considered linear across track:

$$e_1 = \alpha_1(x_a)x_c \quad (2)$$

130 where e_1 is the across track roll error, proportional to the cross-track coordinate x_c .

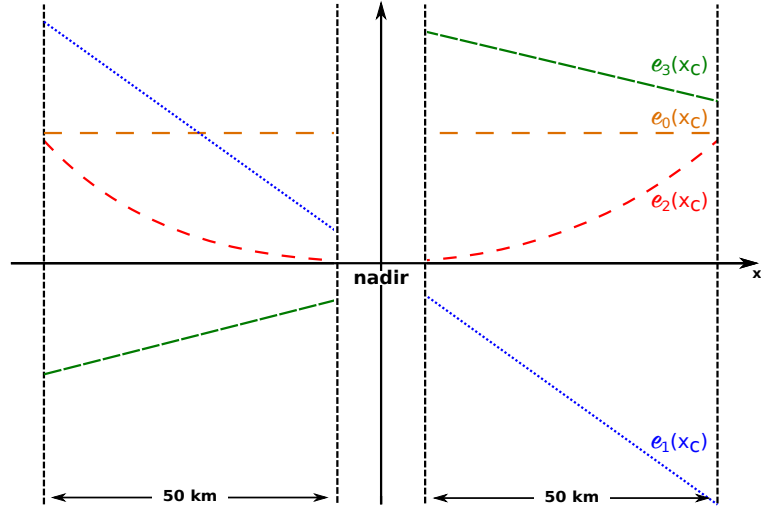


Figure 2. Schematic representation of the SWOT error distributions across track. The errors e_0 , e_1 , e_2 and e_3 correspond respectively to the timing, the roll, the baseline dilatation and the phase errors.

When the baseline of the satellite dilates, the length of the baseline varies which modifies the height measurements. This variation creates a deviation for the calibrated instrument signals at each end of the mast. The baseline dilatation error e_2 is a quadratic function of the cross-track coordinate:

$$e_2 = \alpha_2(x_a)x_c^2 \quad (3)$$

The SWOT interferometric instrument combines signal from two sensors which can have relative phase variations between one another. These variations produce a phase drift which translates into a cross-track linear error, independent in each half-swath. The phase error can thus be written as:

$$e_3 = [\alpha_3(x_a) + \alpha_4(x_a)x_c]\mathcal{H}(-x_c) + [\alpha_5(x_a) + \alpha_6(x_a)x_c]\mathcal{H}(x_c) \quad (4)$$

131 where $\mathcal{H}(x)$ is the Heaviside function which equals 1 when $x > 0$ is true and 0 otherwise.

132 Finally, the variability of water vapor content in the troposphere is a well known source of error
 133 in satellite observations of the ocean also known as the wet-troposphere error (e.g. the missions
 134 AMSR-E [26], Jason 1 [30] and Jason 2 [27]). The wet-tropospheric path delay introduces isotropic
 135 error correlations. However, what we call throughout the present paper the wet-troposphere error
 136 is the residual path delay after a correction performed by a 2-beam radiometer. Since this error is
 137 not structured like the four others described previously, we do not intent to reduce it with the error
 138 reduction method described below.

Under the previous assumptions on the various errors impacting the SWOT data, it is possible to infer the cross-track structure of the total error:

$$e_{\text{total}} = \alpha_0 + \alpha_1x_c + \alpha_2x_c^2 + [\alpha_3 + \alpha_4x_c]\mathcal{H}(-x_c) + [\alpha_5 + \alpha_6x_c]\mathcal{H}(x_c) \quad (5)$$

139 where the explicit dependence of α_i , for $i = 0, \dots, 6$, on x_a has been dropped for the sake of clarity.
 140 Knowing the structure of the total error across track is an important information that can be used to
 141 understand the strong impact of the spatial error correlations on the SWOT signal and to hopefully
 142 reduce some of this impact.

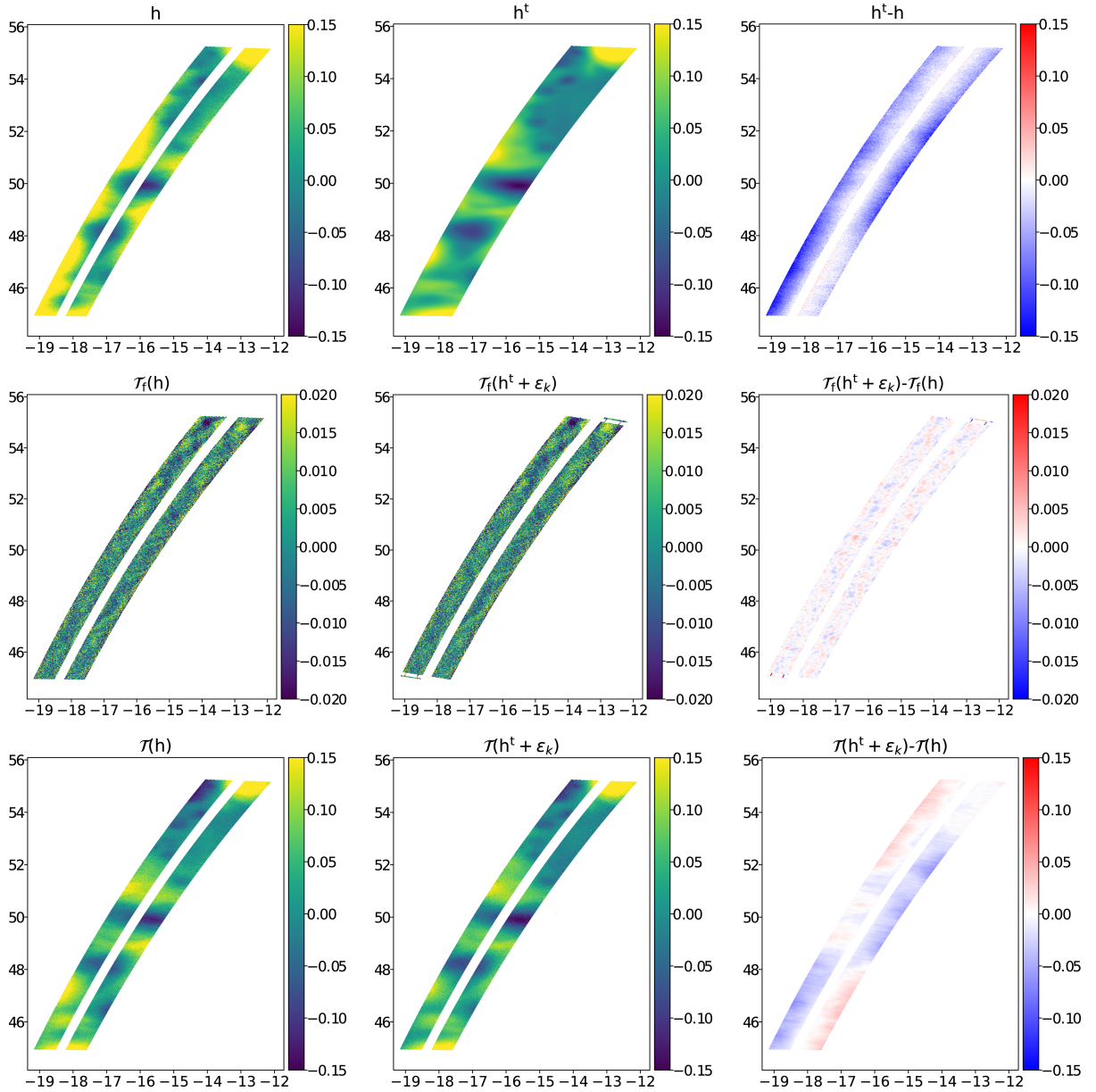


Figure 3. SSH (in meters) on pass 'p031' of cycle 17 given by the true SSH field h^t (first row - left), the SWOT data h (first row - right); the fully detrended (different scale) SWOT data $\mathcal{T}_f(h)$ (second row - left), the fully detrended truth + KaRIn error $\mathcal{T}_f(h^t + \epsilon_k)$ (second row - center) and their difference (second row - right); the partially detrended SWOT data $\mathcal{T}(h)$ (third row - left), the partially detrended truth + KaRIn error $\mathcal{T}(h^t + \epsilon_k)$ (third row - center) and their difference (third row - right).

143 2.2. The error reduction method

144 2.2.1. SWOT data detrending

To reduce the cross-track spatially structured errors described in the previous section, we first propose to project the SWOT signal h in a non-physical space spanned by the spatially structured

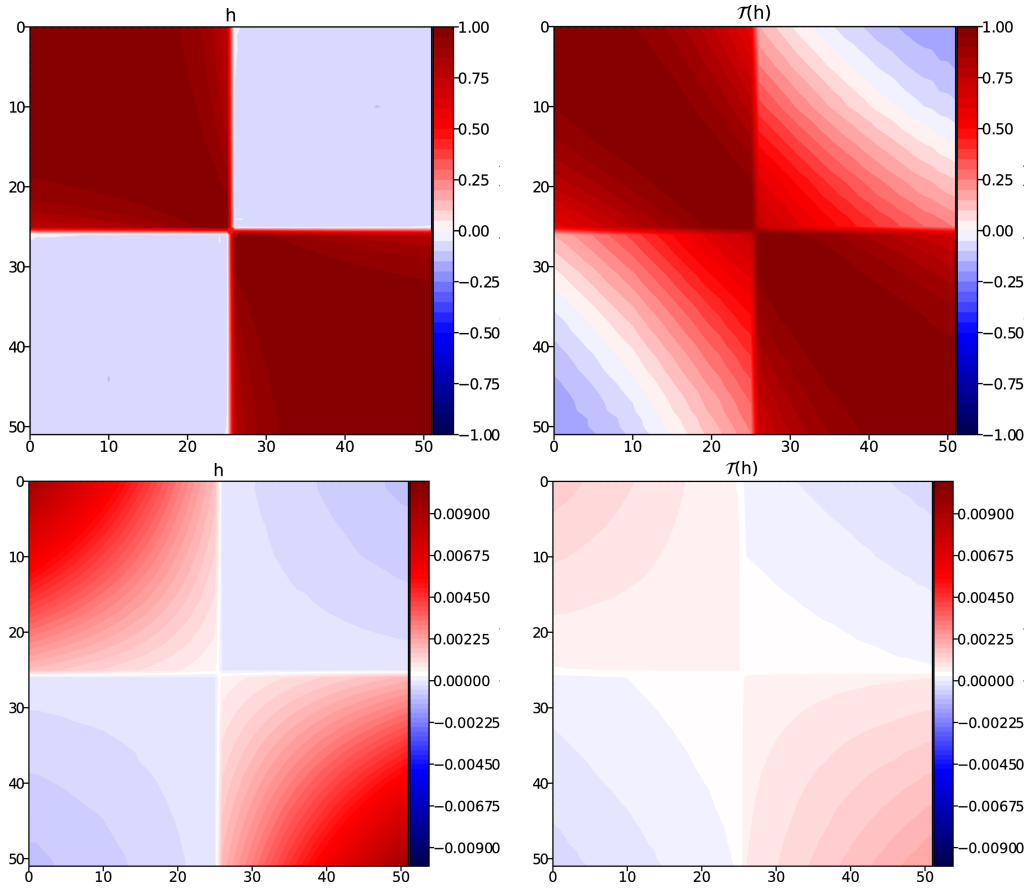


Figure 4. Across track correlations (top) and across track covariances (bottom) of the SWOT data h (left) and the detrended SWOT data $\mathcal{T}(h)$ (right).

errors. Then, the detrending consists in subtracting the projected signal from the across track SWOT signal. The projection coefficients are calculated by minimizing the cost function:

$$\mathcal{J}(\alpha) = \sum_{x_c = -\frac{n_c}{2}}^{\frac{n_c}{2}} \left(h(x_c, x_a) - \{ \alpha_0 + \alpha_1 x_c + \alpha_2 x_c^2 + [\alpha_3 + \alpha_4 x_c] \mathcal{H}(-x_c) + [\alpha_5 + \alpha_6 x_c] \mathcal{H}(x_c) \} \right)^2, \quad (6)$$

145 with n_c the number of across track grid points and with $\alpha = \{ \alpha_0, \alpha_1, \alpha_2, \alpha_3, \alpha_4, \alpha_5, \alpha_6 \}$ are the projection
146 coefficients, functions of x_a .

Having calculated the projection coefficients, the straightforward detrending uses the projection of the SSH $h(x_c, x_a)$, for each along track point x_a :

$$\mathcal{T}_f(h(x_c, x_a)) = h(x_c, x_a) - \{ \alpha_0 + \alpha_1 x_c + \alpha_2 x_c^2 + [\alpha_3 + \alpha_4 x_c] \mathcal{H}(-x_c) + [\alpha_5 + \alpha_6 x_c] \mathcal{H}(x_c) \}. \quad (7)$$

Figure 3, second row-left panel, shows the full detrending $\mathcal{T}_f(h)$ applied to the SWOT observation h (first row-left panel) corresponding to the true ocean state h^t (first row-right panel) on pass 'p031' of cycle 17 in the OSMOSIS region. When comparing the full detrending of the SWOT data to the full detrending of the true signal plus the KaRIn error only (second row-center) and when looking at the difference between the two (second row-right), we can see that the errors are almost entirely removed. However, the full detrending also removes a large part of the large-scale SSH signal. To limit this effect,

we propose a detrending constant along track $\mathcal{T}(h)$ based on the previously computed coefficients averaged over the entire pass:

$$\mathcal{T}(h(x_c, x_a)) = h(x_c, x_a) - \{\tilde{\alpha}_1 x_c + \tilde{\alpha}_2 x_c^2 + [\tilde{\alpha}_3 + \tilde{\alpha}_4 x_c] \mathcal{H}(-x_c) + [\tilde{\alpha}_5 + \tilde{\alpha}_6 x_c] \mathcal{H}(x_c)\}, \quad (8)$$

147 for all x_a and all x_c , where $\tilde{\alpha}_i$ for $i = 1, \dots, 7$ are the along track average of the projection coefficients α_i
 148 computed in Eq. (6). The rationale for this choice is the assumption that the coefficients α_i , for $i \neq 0$,
 149 vary along track with much larger scales than the oceanic features observed by SWOT. In our setup,
 150 we further assumed that the SWOT passes are small enough to consider these coefficients constant
 151 along-track. For longer passes, such an assumption would not hold anymore, and a more sophisticated
 152 approach should be considered. The slow-variation assumption does not hold for the timing error
 153 α_0 . This term is therefore removed from the detrending, Eq. 8, which implicitly means that this error
 154 remains in the detrended SWOT data. The resulting detrended SWOT data $\mathcal{T}(h)$ for pass ‘p003’ at
 155 cycle 17 is shown in the third row-left panel of Fig. 3. A large part of the SSH signal is preserved by the
 156 detrending, yet the large scale errors shown in the difference $h^t - h$ (first row-right) are reduced.

157 Figure 4 shows the across-track correlation (top) and covariance (bottom) matrices for the SWOT
 158 data h (left) and the detrended SWOT data (right). The error covariances (and the variances in
 159 particular) are still present but well reduced by the detrending. The error correlation matrix after
 160 detrending is slightly closer to a diagonal matrix, i.e., the errors are less correlated across track. Finally,
 161 the error correlation matrix after detrending is closer to a Gaussian correlation above and below the
 162 diagonal. Note, that this form of correlation matrix is typical of the wet-troposphere error not taken
 163 into account by the detrending.

164 It is crucial to note that a significant part of the large scale signal has been removed in the
 165 detrended SWOT data and can thus not be directly substituted to an SSH information. Hence, we need
 166 to find a way to correct an actual SSH variable by using the information contained in the detrended
 167 SWOT data. Here, we argue that an appropriate way to address this question comes from data
 168 assimilation techniques.

169 2.2.2. Reducing errors using data assimilation

170 Data assimilation (DA) is a mathematical and methodological approach that allows the
 171 combination of different sources of information on a system and the uncertainties that surrounds them
 172 in order to recover an updated more accurate knowledge of that system. The development and the
 173 application of DA in geosciences is a large and well-settled field of investigation (e.g. [9; 19; 25; 2; 7])
 174 and in particular in oceanographic applications [4; 33; 5; 28; 36]. The main focus of DA so far has been
 175 state and parameter estimation. In the present paper, we propose to use DA to estimate the true SSH
 176 SWOT signal from the detrended SWOT data and constrained by high resolution SSH scenes.

177 The two sources of information that we use in this error reduction method are, on the one hand,
 178 the detrended SWOT data (the observation) and, on the other hand, a high-resolution ensemble of
 179 unrelated (to the truth) SSH fields (the prior). The ensemble of SSH fields is previously interpolated
 180 on the SWOT swath. An ensemble-based DA analysis (e.g. an ensemble Kalman filter, EnKF, see
 181 Appendix B) can then be performed in the “SWOT-space”, i.e., finding a more accurate SWOT estimate
 182 from an ensemble of prior SWOT-like data and the detrended SWOT data.

183 Note that we do not directly replace the SWOT data by the detrended SWOT data in the SSH
 184 state space, which would be mathematically incorrect, we rather perform the assimilation in the
 185 non-physical detrended space. In practice, this means that an observation operator is created to link
 186 the variations of the prior ensemble and the variations of the SWOT data in the detrended space and
 187 use that information to correct an actual SSH. In other words, this error reduction method can be seen
 188 as an optimal interpolation scheme [9, Section 4.2] but with a prior error covariance matrix given by
 189 high-resolution SSH scenes.

190 It is also possible to apply the same method but using different observations instead of using
 191 the detrended SWOT data. For instance, in the numerical experiments below, this is done using
 192 successively the original SWOT data, the nadir data and the nadir-adjusted detrended SWOT data
 193 (defined in Section 3.3). Since most DA schemes make the assumption of uncorrelated observation
 194 errors and since the detrending reduces the SWOT error correlations, we here expect that an
 195 assimilation of the detrended SWOT data \mathcal{T} defined by Eq. 8 will be much more efficient than
 196 the straightforward SWOT data assimilation.

Notations and markers		
Truth	h^t	Dashed black line
SWOT observation	h	Dashed red line
Gaussian filtered SWOT	$\mathcal{G}(h)$	Dotted red line
SWOT DA	DA[h]	Grey
Detrended SWOT DA	DA[$\mathcal{T}(h)$]	Blue
Nadir DA	DA[nadir]	Orange
Nadir-adjusted detrended SWOT DA	DA[$\mathcal{U}(\mathcal{T}(h))$]	Green

Table 2. Glossary of the variable names and markers for the experimental results.

197

198 3. Results

199 3.1. The experimental set up

200 The synthetic SWOT data are generated from hourly outputs of the NATL60 simulation between
 201 October 1, 2012 and September 30, 2013. The OSMOSIS region as considered in this study is visited
 202 by 28 passes per satellite cycle, with a total of 18 cycles over the year. The numerical experiments are
 203 carried out for the first three passes ('p003', 'p031' and 'p059') of all 18 cycles, which amounts to a total
 204 of 54 SWOT datasets.

205 The error reduction method described in Section 2.2.2 is performed with an EnKF analysis
 206 (Appendix B), using a static ensemble made of 60 SSH fields randomly picked in the simulation
 207 between June 16, 2012 and August 31, 2012. The specific DA parameters are detailed in Appendix C.

208 Comparisons are performed between the true state of the ocean in the swath – which would
 209 correspond to an error free SWOT observation – and the SWOT estimations: the original SWOT data
 210 (from the SWOT simulator), the SWOT data filtered with a Gaussian filter, the results of DA using
 211 the SWOT data, the detrended SWOT data, the SWOT nadir and the detrended SWOT data adjusted
 212 by the nadir (this adjustment is described in Section 3.3). See Table 2 for a glossary of the compared
 213 variables. The Gaussian filter is applied to the original SWOT data that has been inpainted using
 214 a bivariate spline approximation in order to close the gap. The Gaussian filter is used with a 6-km
 215 standard deviation and has a smoothing effect that reduces the very small scale errors, in particular
 216 the KaRIn errors. Hence, in addition to the original SWOT data, the comparison to the SWOT data
 217 filtered with a Gaussian filter allows to only assess the error reduction method on the large scales.

218 The error reduction methods are illustrated with a focus on one specific pass, and are assessed
 219 using the 54 SWOT scenes with root-mean-square errors (RMSE) and spectral diagnostics. RMSE
 220 scores on SSH are computed by cross-track coordinate, and globally. Global RMSEs are also computed
 221 for SSH gradients and Laplacian (relative vorticity). Spectral diagnostics include along and across
 222 track power spectrum densities and spectral coherences.

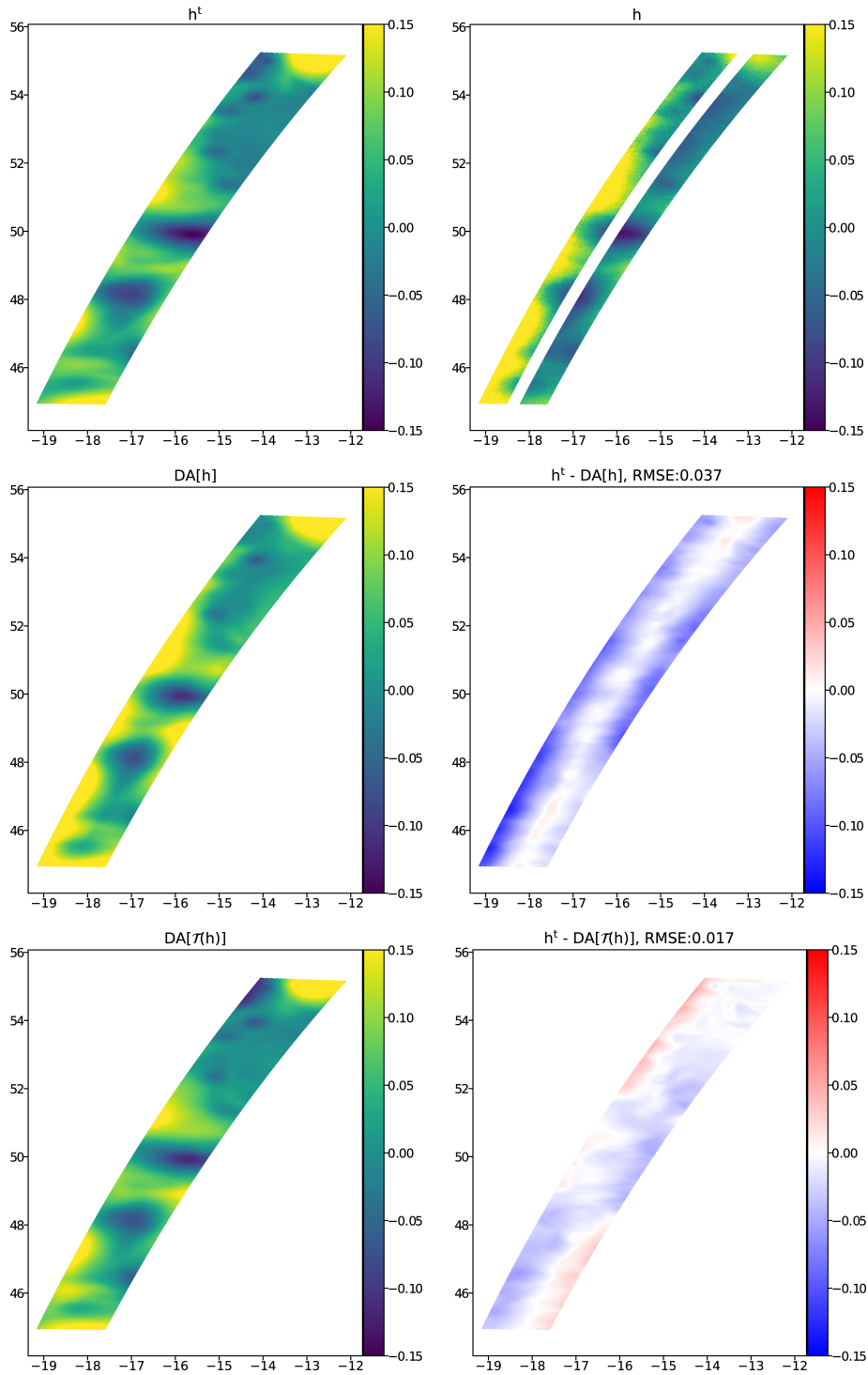


Figure 5. SSH on pass 'p031' of cycle 17 given by the truth h^t (top-left), the SWOT data h (top-right); and the results $DA[h]$ (middle-left) and $DA[\mathcal{T}(h)]$ (bottom-left) with their differences to h^t (middle-right and bottom-right, resp.).

223 3.2. Error reduction by assimilating detrended SWOT data

224 Figure 5 displays an illustration on 'p031' at cycle 17, of the error reduction method assimilating
 225 the original SWOT data ($DA[h]$) and the detrended SWOT data ($DA[\mathcal{T}(h)]$). The two top-row panels,
 226 showing the truth h^t and the SWOT data h , are identical to those in Figure 3. The second and third
 227 rows show the results of the error reduction method ($DA[h]$ and $DA[\mathcal{T}(h)]$ resp.), on the left panels,

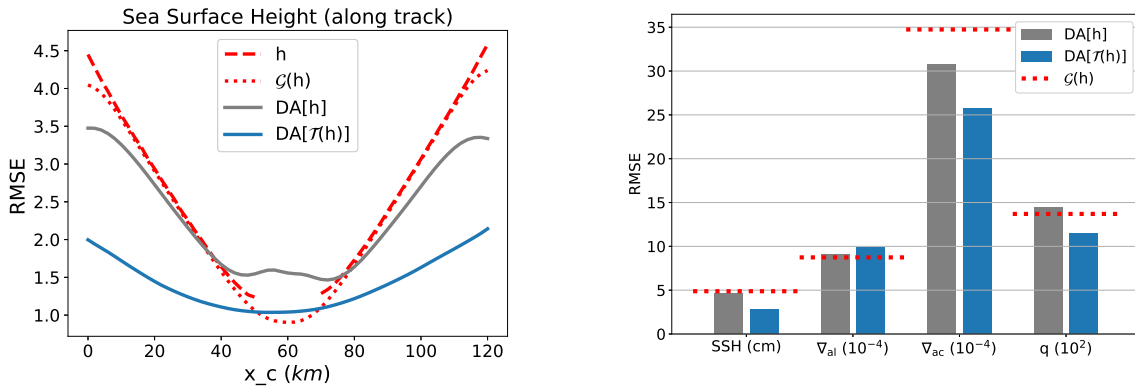


Figure 6. Left: Along track RMSE over the 54 passes on SSH (cm) of h , $\mathcal{G}(h)$, $DA[h]$ and $DA[\mathcal{T}(h)]$ against h^t (see Table 2 for notations). Right: Global RMSE on SSH (cm), along and across track gradients ∇_{al} and ∇_{ac} resp. (scaled by 10^{-4}) and relative vorticity q (scaled by 10^2).

228 and the point-wise differences of those results to the truth ($h^t - DA[h]$ and $h^t - DA[\mathcal{T}(h)]$ resp.), on the
 229 right panels. Using the detrended SWOT data rather than SWOT in the error reduction method shows a
 230 clear improvement. The RMSE, for this pass, gives an accuracy increase of more than 50%.

231 The two error reduction methods are applied to the 54 SWOT passes. Figure 6 shows along track
 232 RMSE (left panel) and global RMSE on SSH, along and across track gradients and relative vorticity
 233 (right panel). As expected, the SWOT cross-track errors on SSH (red dashed line) are larger close
 234 to the outside edges of the double-swath. Applying a Gaussian filter to SWOT ($\mathcal{G}(h)$, red dotted
 235 line) does not reduce these strong cross-track errors. Assimilation of the raw SWOT data (grey
 236 line) reduces marginally the errors close to the edges of the swath and does not well recover the
 237 gap between the half-swathes. The cross-track error reduction of the detrended SWOT DA is more
 238 substantial, especially close to the edges of the swath. It must be noted though that the inpainting
 239 combined with Gaussian filtering shows better error reduction at the very center of the gap. Following
 240 the global RMSE diagnostics (Figure 6, right panel), the improvement by the detrended SWOT DA is
 241 confirmed on the SSH, the across track gradient ∇_{ac} and the relative vorticity q . Notably, the good
 242 RMSE reduction on SSH is confirmed over all passes with an approximated 50% reduction. The RMSE
 243 of $DA[\mathcal{T}(h)]$ slightly increases on the along track gradient. Indeed, the assimilation of the detrended
 244 SWOT data may have a slight smoothing effect which can degrade the gradients. Since the error
 245 reduction method does not correct much in the along track direction, this smoothing effect becomes
 246 visible.

247 Spectral diagnostics have also been performed. Figure 7 (top panels) shows the SSH power
 248 spectral density computed along (left) and across (right) track. Both the Gaussian filtered SWOT data
 249 and the detrended SWOT DA recover the true h^t along track spectral density (dashed black line)
 250 to 25km scales. The across track spectral densities of SWOT, Gaussian filtered SWOT data and $DA[h]$
 251 are over energetic in the large scales (over 100km scales). When using the detrended SWOT data,
 252 the error reduction method manages to estimate the correct energy throughout the spectra down to 25km
 253 scales. In terms of spectral coherence (Figure 7, bottom panels) the estimations are degraded under the
 254 50km scales. Once again, the assimilation tends to smooth some structures which results in no spectral
 255 coherence improvement under 50km scales and, moreover, a slight spectral coherence degradation at
 256 all scales in the along track direction. Nonetheless, a large across track spectral coherence improvement
 257 is made in the large scales.

258 3.3. Combining nadir and SWOT data

259 In this experiment, we assess the improvements that can be obtained by the introduction of
 260 another source of information: the SWOT nadir data.

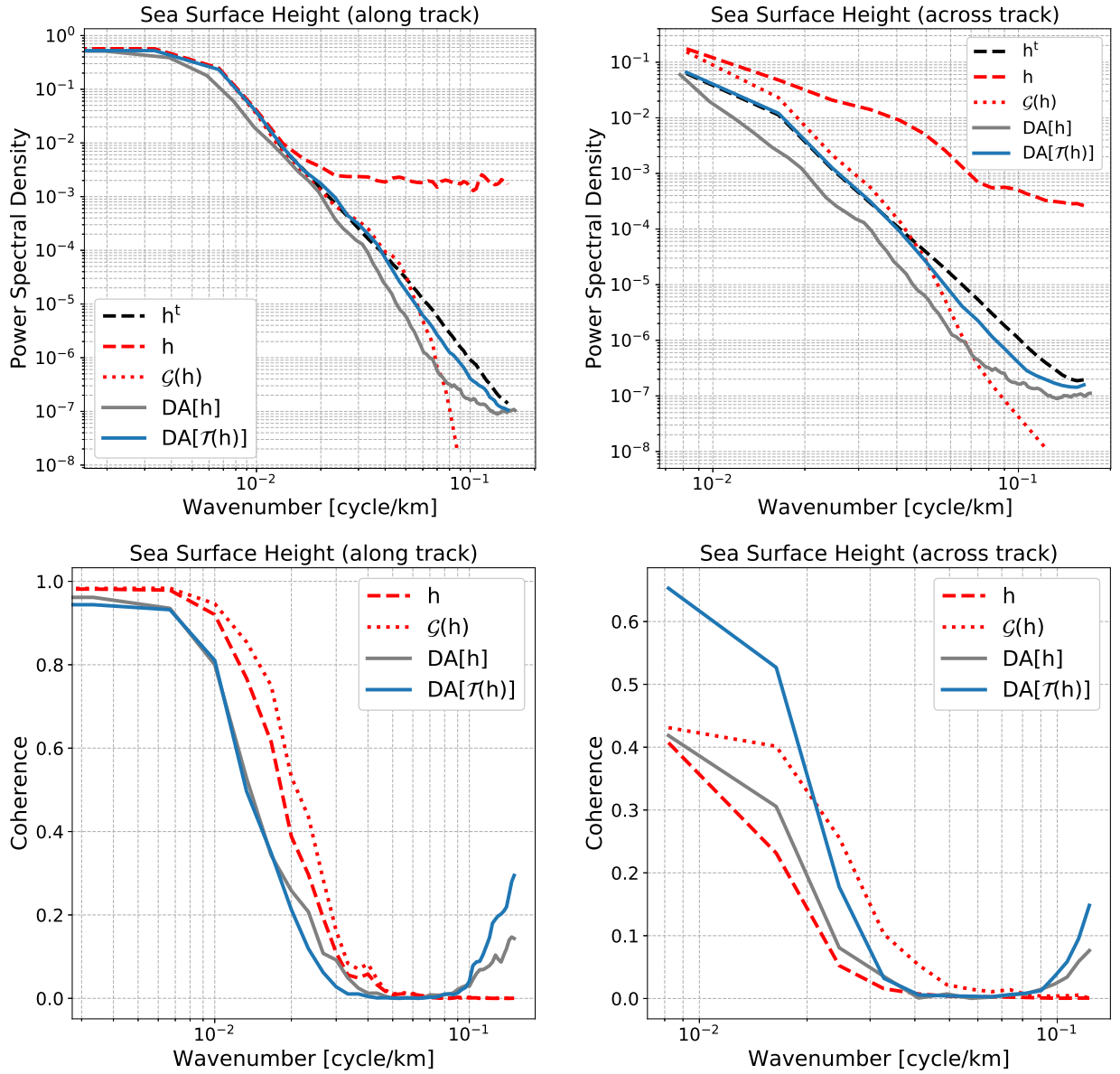


Figure 7. Top: Power spectral density along (left) and across (right) track, in function of spatial frequency (km^{-1}), over the 54 passes on SSH (cm) of h^t , h , $\mathcal{G}(h)$, $\text{DA}[h]$ and $\text{DA}[\mathcal{T}(h)]$ (see Table 2 for notations). **Bottom:** Same as top but spectral coherence against h^t .

As mentioned in Section 2.2.1, the SWOT data detrending \mathcal{T} defined in Eq. (8) does not take into account the constant term \tilde{a}_0 . This constant term was omitted in order to avoid removing a non-zero SSH signal average. Here, we use the nadir information in order to remove the error-generated non-zero SWOT average while preserving the SSH signal average. In practice, we compute the nadir-adjusted detrending as follows:

$$\mathcal{U}(\mathcal{T}(h)) = \mathcal{T}(h) - w \cdot (\overline{\mathcal{T}(h)} - \overline{\text{nadir}}) \quad (9)$$

261 where $\overline{\mathcal{T}(h)}$ and $\overline{\text{nadir}}$ are, respectively, the detrended SWOT data average and the nadir data
 262 average (over the pass) and where w is a prescribed weight (hereunder, $w = 0.6$) representing
 263 the SWOT/nadir error ratio. The error reduction method based on the nadir-adjusted detrended
 264 SWOT data is noted $\text{DA}[\mathcal{U}(\mathcal{T}(h))]$. We also implemented, the error reduction method using the nadir
 265 data only: $\text{DA}[\text{nadir}]$. Other experiments (not shown here) have been performed by assimilating

266 simultaneously the detrended SWOT data and the nadir data but the assimilation of the nadir degraded
 267 the performances especially at the small scales.

268 Figure 8 shows the illustration pass ‘p003’ at cycle 17, introduced in Figure 5, comparing two
 269 additional results: DA[nadir] and DA[$\mathcal{U}(\mathcal{T}(h))$]. The illustration seems to suggest that the error
 270 reduction method using the nadir data only partly recovers the large scale errors but fails to capture the
 271 smaller scales. Meanwhile, combining the nadir data with the detrended SWOT data, i.e. DA[$\mathcal{U}(\mathcal{T}(h))$]
 272 versus DA[$\mathcal{T}(h)$], improves the error reduction. This result is confirmed in Figure 9 which, similarly
 273 to Figure 6, shows the along-track (left) and global (right) RMSE assessing the two additional results.
 274 Interestingly, the DA[nadir] errors plotted across track are very close to the SWOT errors. This across
 275 track shape of the DA[nadir] errors is due to the localization technique used in the assimilation scheme:
 276 the SSH corrections due to the assimilation fade out with the distance to the nadir. At the center of the
 277 track ($x_c = 60$ km), the nadir data are accurate (only nadir altimeter error and troposphere error) and
 278 the assimilation analysis manages to recover information left and right of the nadir.

279 The main result here is that combining nadir and SWOT by adjusting the detrended SWOT data
 280 with the nadir helps reducing SSH RMSE. In particular, there is a gain in accuracy at the center of the
 281 track where the estimate of the error reduction method is now more accurate than the Gaussian filtered
 282 SWOT data $\mathcal{G}(h)$. This gain appears as well in the global SSH RMSE.

283 Finally, the spectral analysis in Figure 10 confirms the poor capability of a nadir (alone)
 284 assimilation to recover a two-dimensional signal. However, the use of the nadir to adjust the detrended
 285 SWOT data for the error reduction method DA[$\mathcal{U}(\mathcal{T}(h))$] slightly improves the power spectral densities
 286 and the spectral coherences.

287 4. Discussion

288 The data from the future SWOT, wide-swath ocean altimetry mission are expected to be impacted
 289 by large, spatially structured and correlated errors. If we want to reach the degree of accuracy and
 290 resolution made theoretically achievable by the SWOT system configuration, we need to reduce these
 291 errors and their correlations.

292 Based on the current knowledge of the expected SWOT errors and their cross-track structure, we
 293 propose an error reduction method to remove the part of the SWOT signal that exhibits signatures
 294 identical to the structured errors. This results in a new, detrended SSH signal that is non fully physical
 295 (since a part of the physical signal might be removed as well), but much less affected by structured
 296 errors. In conjunction with the detrending, we also propose a SWOT error reduction method based
 297 on a static ensemble data assimilation (DA). Ensemble DA is used to combine the detrended SWOT
 298 data information to the information from an independent ensemble of scenarios (e.g. high resolution
 299 model fields or reanalysis). The detrended SWOT data are particularly suited to this error reduction
 300 method (or more generally to DA) due to the reasonably small spatial correlations in their residual
 301 errors. It is indeed common practice in DA to assume the observation errors uncorrelated, and many
 302 DA softwares are hard-coded under this assumption. The proposed SWOT detrending can also be
 303 incorporated in a fully integrated DA scheme, by convolving it to the existing observation operator:
 304 $\mathcal{H} \equiv \mathcal{T} \circ \mathcal{H}$. This should significantly improve the assimilation.

305 The efficiency of the error reduction method using detrended SWOT data has been assessed with
 306 an observing system simulation experiment and using diagnostics on the physical SSH fields (RMSEs)
 307 and their spectral characteristics (power spectra and coherence). This method has been compared to
 308 the raw SWOT data, to the Gaussian filtered SWOT data and to the error reduction method using
 309 directly the SWOT data (i.e., without detrending). Most diagnostics show the good performance of
 310 the proposed method for the retrieval of SSH on the SWOT swath. Notably, the method recovers the
 311 energy of the signal throughout the spectra down to 25km scales. However, in this work, because the
 312 SWOT scenes were not spatially extended, we neglected the along-track variations of the structured
 313 errors. But they may explain the relatively poor results of the error reduction method in the diagnostics
 314 based on an along-track processing (RMSE in along-track SSH gradient, and along-track spectral

315 coherence). Also, the error reduction method developed in this work addresses the structured errors
316 due to the satellite design, but not other errors that may show spatial correlations, e.g. errors due
317 to the atmospheric water vapor. These errors were neglected in this paper, but methods exist to
318 account for them [3,35,38]. The next step should then focus on diagnosing the residual observation
319 error correlations, and check whether it is possible to account for them in the assimilation. Finally,
320 the performance of ensemble DA partly depending on the quality of the initial ensemble, a natural
321 perspective of improvement of the method lies in the improvement of the initial ensemble itself. Using
322 seasonally-varying ensembles for the timely processing of SWOT data would be a first, easy step.
323 Integrating the detrending procedure in a full DA system would represent the ultimate goal.

324 The SWOT nadir data can be combined with the error reduction method to improve the accuracy
325 of the SWOT wide-swath estimation. In the last section of the numerical experiments, we introduced
326 the SWOT nadir data in the method. Even though the use of the nadir data has been rather minimalist,
327 it further improves the error reduction method performance. Yet, with the simple DA configuration
328 used in this exploratory work, the combined assimilation of the nadir data and the detrended SWOT
329 data resulted in destructive interferences (not shown). We did not tackle this technical DA issue here,
330 not to deviate from our primary focus, the wide-swath data. But it will have to be done if the error
331 reduction method is selected for operational applications in the future.

332 Although the experiments presented in this paper are based on an advanced observing system
333 simulation experiment, further validations before operational applications are required. It should be
334 noted that the experiments presented in this study are based on synthetic SWOT observations from a
335 state-of-the-art high resolution submesoscale permitting ocean model simulation (NEMO-NATL60).
336 However, this model simulation does not account for the high frequency internal tides that will affect
337 SWOT SSH signals at scales <100km [22,34]. It is unclear how the performance of the ensemble DA
338 experiments presented in this study would be affected by the representation of high frequency internal
339 tides in the model. Future studies using an upcoming similar simulation that will include internal
340 tides should soon be performed.

341 5. Conclusions

342 The present paper is a proof-of-concept, for the future SWOT data pre-processing, showing that
343 an error reduction method based on the detrending of the spatially structured errors and the retrieval
344 of the large scale physical signal with ensemble data assimilation, can help recover a large part of the
345 SWOT SSH signal. Notably, the detrending step of the method is an innovation in itself that can be
346 separately incorporated in an operational data assimilation scheme and enhance its performance. This
347 paper should therefore be seen as a first demonstration for a method that can be further improved and
348 could ultimately be used operationnaly. The method leads to accurate estimations of the SSH signal
349 and allowed the retrieval of the spectral energy down to the 25km scales.

350 Further developments are needed in order to improve the method and to reduce the errors at
351 finer scales. The first step of the method, the detrending, could be improved by accounting for the
352 along-track variations of the structured errors with, for instance, an along-track processing of the
353 detrending coefficients. Also, the two-dimensional structured errors such as the wet-troposphere
354 errors are not taken into account in the detrending process. Hence, a two-dimensional detrending or
355 a combination of the current cross-track detrending and other existing methods [3,35,38] should be
356 investigated. The second step of the method, the retrieval, could be improved by using a larger and/or
357 a more appropriate ensemble of SSH scenes, for instance, a seasonally-varying ensemble. A craftier
358 methodology for combining the two-dimensional SWOT data with the SWOT nadir data should also
359 be studied. Finally, in order to further strengthen the validation of the method, an assessment of
360 its capacity to recover the SSH SWOT signal in an experimental set up that includes high frequency
361 internal tides should be performed.

362 **Author Contributions:** Sammy Metref, Emmanuel Cosme and Julien Le Sommer designed the study; Sammy
363 Metref, Emmanuel Cosme, Julien Le Sommer and Jean-Michel Brankart designed the numerical experiments; Nora

364 Poel and Laura Gómez Navarro provided the SWOT related implementation tools; Sammy Metref, Emmanuel
 365 Cosme, Julien Le Sommer and Jean-Michel Brankart contributed to the analysis of the results; Sammy Metref led
 366 the redaction of the manuscript and all authors contributed to the writing.

367 **Funding:** This research was funded by ANR (project number ANR-17-CE01-0009-01) and CNES through the
 368 OST/ST and the SWOT Science Team.

369 **Acknowledgments:** The authors thank Maxime Ballarotta and Clément Ubelmann from CLS for the constructive
 370 discussions related to this study.

371 **Conflicts of Interest:** The authors declare no conflict of interest. The funders had no role in the design of the
 372 study; in the collection, analyses, or interpretation of data; in the writing of the manuscript, or in the decision to
 373 publish the results.

374 Appendix A SWOT simulator detailed parameters

375 Hereunder is the SWOT simulator parameter file creating the synthetic SWOT data (Section 2.1)
 376 used in the numerical experiments:

```

377 # — Orbit file :
378 # Name of the orbit file
379 satname = "swot292"
380 filesat=dir_setup+ os.sep + 'orbit292.txt'
381
382 # —————#
383 # SWOT swath parameters
384 # —————#
385 # — Distance between nadir and the end of the swath (in km):
386 halfswath = 60.
387 # — Distance between nadir and the beginning of the swath (in km):
388 halfgap = 10.
389 # — Along track resolution (in km):
390 delta_al = 2.
391 # — Across track resolution (in km):
392 delta_ac = 2.
393 # — Shift longitude of the orbit file if no pass is in the domain
394 # (in degree): Default value is None (no shift)
395 shift_lon = None
396 # — Shift time of the satellite pass (in day):
397 # Default value is None (no shift)
398 shift_time = None
399
400 # —————#
401 # Model input parameters
402 # —————#
403 # — Type of grid:
404 grid = 'irregular'
405 # — Time step between two model outputs (in days):
406 timestep = 1./24.
407 # — Number of outputs to consider:
408 # (timestep*nstep=total number of days)
409 nstep = 365.*24.
410
411 # —————#
412 # SWOT output files
413 # —————#
414 interpolation = 'linear'
415
416 # —————#
417 # SWOT error parameters
418 # —————#
419 # — KaRIn noise (True to compute it):
420 KaRIn = True
421 # — SWH for the region:
422 swh = 2.0
423

```

```

424 # — Number of km of random coefficients for KaRIn noise:
425 nrandKaRIn = 1000
426
427 # — Other instrument error (roll , phase , baseline dilation , timing)
428 ## -----
429 # — Compute nadir (True or False):
430 nadir = True
431 # — Number of random realisations for instrumental and geophysical
432 #   error (recommended ncomp=2000), ncomp1d is used for 1D spectrum ,
433 #   and ncomp2d for 2D spectrum (wet troposphere computation):
434 ncomp1d = 2000
435 ncomp2d = 2000
436 # — Cut off frequency:
437 lambda_cut = 20000
438 lambda_max = 20000
439 # — Roll error (True to compute it):
440 roll = True
441 # — Phase error (True to compute it):
442 phase = True
443 # — Baseline dilation error (True to compute it):
444 baseline_dilation = True
445 # — Timing error (True to compute it):
446 timing = True
447
448 ## — Geophysical error
449 ## -----
450 # — Wet tropo error (True to compute it):
451 wet_tropo = True
452 # — Beam print size (in km):
453 #   Gaussian footprint of sigma km
454 sigma = 8.
455 # — Number of beam used to correct wet_tropo signal (1, 2 or 'both'):
456 nbeam = 2
457 # — Beam position if there are 2 beams (in km from nadir):
458 beam_pos_l = -35.
459 beam_pos_r = 35.

```

461 Appendix B Ensemble Kalman filter brief description

The ensemble Kalman filter [14] a stochastic alternative to the deterministic Kalman filter. For high dimension systems, the propagation in time of the information and the size of the problem to solve makes the standard Kalman filter [24] untracktable. The EnKF partly solves those issues using a Monte Carlo approach. The error covariances are propagated with an ensemble of scenarios propagated by a model (not in our particular case, where the ensemble is static in time). The analysis step of the standard Kalman filter is then computed but using the statistical prior error covariance matrix and gives an updated state of the system:

$$x^a = x^f + K(y - x^f) \quad (\text{A1})$$

462 where x^f is the prior state of the system, y is the observation and K is the Kalman gain matrix
463 that depends on the prior error covariance matrix, the observation error covariance matrix and the
464 observation operator.

465 In order to account for the undersampling of the ensemble in the representation of the prior error
466 covariance matrix, it is often mandatory to perform a localization in the DA scheme which reduces the
467 impact of long-distance observations.

468 Appendix C Data assimilation set up details

- 469 • The observation error covariance matrices, \mathbf{R} , were not specifically tuned. They are assumed
 470 diagonal and constant along the diagonal: $\mathbf{R} = \text{diag}(\sigma_Y)$. The respective values of σ_Y are detailed
 471 in Table A1.

Y	h	$\mathcal{T}(h)$	nadir	$\mathcal{U}(\mathcal{T}(h))$
σ_Y	0.08	0.03	0.01	0.02

Table A1. Values of σ_Y defining the observation error covariance matrices $\mathbf{R} = \text{diag}(\sigma_Y^2)$, in meters, for the respective observations Y.

- 472
- 473 • The localization used in the ensemble Kalman Filter is the domain localization described in [23].
 474 The localization parameters, namely the localization cutoff and radius, are specified for each
 475 observation in Table A2.

Y	h	$\mathcal{T}(h)$	nadir	$\mathcal{U}(\mathcal{T}(h))$
ρ_{cut}	80	80	80	80
ρ_{loc}	40	40	60	40

Table A2. Localization cutoff ρ_{cut} and radius ρ_{loc} , in km, for the respective observations Y.

476

477 References

- 478 1. Amores A., Jordá G., Arsouze T., Le Sommer J. 2018. Up to what extent can we characterize ocean eddies
 479 using present-day gridded altimetric products? *J. of Geo. Res.: Oceans*, **123(10)**: 7220-7236.
- 480 2. Asch M., Bocquet M., Nodet M. 2016. *Data Assimilation: Methods, Algorithms, and Applications*. Fundamentals
 481 of Algorithms. SIAM, Philadelphia.
- 482 3. Brankart, J. M., Ubelmann C., Testut C.E., Cosme E., Brasseur P., Verron J. 2009. Efficient parameterization of
 483 the observation error covariance matrix for square root or ensemble Kalman filters: application to ocean
 484 altimetry. *Monthly Weather Review*, **137(6)**, 1908-1927.
- 485 4. Bennett A.F.. 1992. *Inverse Methods in Physical Oceanography*. Cambridge University Press, Cambridge, UK
 486 and New York, NY, USA.
- 487 5. Bertino L., Evensen G., Wackernagel H. 2003. Data assimilation in the geosciences: An overview of methods,
 488 issues, and perspectives. *International Statistical Review*, **71(2)**, 223-241.
- 489 6. Buckingham C.E., Naveira Garabato A.C., Thompson A.F., Brannigan L., Lazar A., Marshall D.P., ... Belcher
 490 S.E. 2016. Seasonality of submesoscale flows in the ocean surface boundary layer. *Geophysical Research Letters*,
 491 **43(5)**, 2118-2126.
- 492 7. Carrassi A., Bocquet M., Bertino L., Evensen G. 2018. Data assimilation in the geosciences: An overview of
 493 methods, issues, and perspectives. *WIREs Clim. Change* 2018, **9(5)**.
- 494 8. Chelton D.B., Schlax M.G., Samelson R.M., Farrar J.T., Molemaker M.J., McWilliams J.C., Gula J. 2018.
 495 Prospects for future satellite estimation of small-scale variability of ocean surface velocity and vorticity.
 496 *Progress in Oceanography*.
- 497 9. Daley R. 1991. *Atmospheric data analysis*. Cambridge University Press, Cambridge, United Kingdom.
- 498 10. Dibarboure G. and Ubelmann C. 2014. Investigating the performance of four empirical cross-calibration
 499 methods for the proposed SWOT mission. *Remote Sensing*. **6(6)**: 4831-4869.
- 500 11. Ducouso N., Le Sommer J., Molines J.M., Bell M. 2017. Impact of the "Symmetric Instability of the
 501 Computational Kind" at mesoscale-and submesoscale-permitting resolutions. *Ocean Modelling*. **120**: 18-26.
- 502 12. Durand M., Fu L.L., Lettenmaier D., Alsdorf D., Rodriguez E., Esteban-Fernandez D. 2010. The Surface
 503 Water and Ocean Topography Mission: Observing terrestrial surface water and oceanic submesoscale eddies.
 504 *Proc. IEEE*. **98**: 766-779.

- 505 13. Esteban-Fernandez, D. 2014. SWOT project mission performance and error budget document. *JPL Doc.* JPL
506 D-79084. Rapp. tech. JPL, NASA.
- 507 14. Evensen G. 2009. *Data Assimilation: The Ensemble Kalman Filter*. Springer- Verlag/Berlin/Heidelberg, second
508 edn.
- 509 15. Fresnay S., Ponte A.L., Le Gentil S., Le Sommer J. 2018. Reconstruction of the 3-D Dynamics From Surface
510 Variables in a High-Resolution Simulation of North Atlantic *J. of Geo. Res.: Oceans*, **123**(3): 1612-1630.
- 511 16. Fu L.L. and Ferrari R. 2008. Observing oceanic submesoscale processes from space. *Eos, Trans. Amer. Geophys.*
512 *Union*, **89**: 488.
- 513 17. Fu L.L., Alsdorf D., Rodriguez E., Morrow R., Mognard N., Lambin J., ... Lafon T. 2009, March. The SWOT
514 (Surface Water and Ocean Topography) Mission: spaceborne radar interferometry for oceanographic and
515 hydrological applications. In *OCEANOBS'09 Conference*.
- 516 18. Gaultier L., Ubelmann C., Fu L.L. 2015. SWOT Simulator Documentation, *Tech. Rep. 1.0.0*, Jet Propulsion
517 Laboratory, California Institute of Technology: Pasadena, CA, USA, 2015.
- 518 19. Ghil M. and Malanotte-Rizzoli P. 1991. Data assimilation in meteorology and oceanography. *Adv. Geophys.*,
519 **33**: 141-266.
- 520 20. Gómez-Navarro L., Fablet R., Mason E., Pascual A., Mourre B., Cosme E., Le Sommer J. 2018. SWOT Spatial
521 Scales in the Western Mediterranean Sea Derived from Pseudo-Observations and an Ad Hoc Filtering.
522 *Remote Sensing*, **10**(4), 599.
- 523 21. Gómez Navarro L., Cosme E., Le Sommer J., Papadakis N., Pascual A. In prep. To be defined. *To be defined*,
524 To be defined.
- 525 22. Gula J., Blacic T.M., Todd R.E. 2019. Submesoscale coherent vortices in the Gulf Stream. *Geophysical Research*
526 *Letters*, **46**.
- 527 23. Hunt B., Kostelcic E.J., Szunyogh I. 2007. Efficient data assimilation for spatiotemporal chaos: A local
528 ensemble transform Kalman filter. *Physica D*, **230**: 112-126.
- 529 24. Kalman R.E. 1960. A new approach to linear filtering and prediction problems. *Journal of basic Engineering*,
530 **82**(1): 35-45.
- 531 25. Kalnay E. 2003. *Atmospheric modeling, data assimilation and predictability*. Cambridge university press.
- 532 26. Kawanishi T., Sezai T., Ito Y., Imaoka K., Takeshima T., Ishido Y., ... , Spencer R.W. 2003. The Advanced
533 Microwave Scanning Radiometer for the Earth Observing System (AMSR-E), NASDA's contribution to the
534 EOS for global energy and water cycle studies. *IEEE Transactions on Geoscience and Remote Sensing*, **41**(2):
535 184-194.
- 536 27. Lambin J., Morrow R., Fu L.L., Willis J.K., Bonekamp H., Lillibrige J., ... , Parisot F. 2010. The OSTM/Jason-2
537 mission. *Marine Geodesy*, **33**(S1): 4-25.
- 538 28. Lermusiaux P.F.J. 2006. Uncertainty estimation and prediction for interdisciplinary ocean dynamics. *J. Comp.*
539 *Phys.*, **217**: 176-199.
- 540 29. Madec, G. 2015. NEMO ocean engine. *Note du Pôle de modélisation*, Institut Pierre-Simon Laplace (IPSL),
541 France, No 27, ISSN No 1288-1619.
- 542 30. Ménard Y., Fu L.L., Escudier P., Parisot F., Perbos J., Vincent P., ... , Kunstmann G. 2003. The Jason-1 mission
543 special issue: Jason-1 calibration/validation. *Marine Geodesy*, **26**(3-4), 131-146.
- 544 31. NATL60 configuration on GitHub. Available online doi: 10.5281/zenodo.1210116 (accessed on 12 April
545 2019).
- 546 32. Oke P.R., Brassington G.B., Griffin D.A., Schiller A. 2010. Ocean data assimilation: a case for ensemble
547 optimal interpolation. *Austr. Meteorol. and Oc. Journal*, **59**(Sp. Iss), 67-76.
- 548 33. Pham D.T., Verron J., Roubaud M.C. 1998. A singular evolutive extended Kalman filter for data assimilation
549 in oceanography. *J. of Marine Syst.*, **16**(3-4), 323-340.
- 550 34. Qiu B., Chen S., Klein P., Wang J., Torres H., Fu L.L., Menemenlis D. 2018. Seasonality in transition scale
551 from balanced to unbalanced motions in the world ocean. *J. of Phys. Ocean.*, **48**(3), 591-605.
- 552 35. Ruggiero G.A., Cosme E., Brankart J. M., Le Sommer J., Ubelmann C. 2016. An efficient way to account
553 for observation error correlations in the assimilation of data from the future swot high-resolution altimeter
554 mission. *Journal of Atmospheric and Oceanic Technology*, **33**(12), 2755-2768.
- 555 36. Sakov P., Counillon F., Bertino L., Lisaeter K.A., Oke P.R., Korabely A. 2012. Topaz4 : an ocean-sea ice data
556 assimilation system for the north atlantic and arctic. *Ocean Sci.*, **8**: 633-656.

- 557 37. SWOT simulator on GitHub. Available online: <https://github.com/SWOTsimulator> (accessed on 12 April
558 2019).
- 559 38. Yaremchuk M., D'Addezio J.M., Panteleev G., Jacobs G. 2018. On the approximation of the inverse error
560 covariances of high-resolution satellite altimetry data. *Q. J. R. Meteorol. Soc.*, **144(715)**: 1995-2000.

561 **Sample Availability:** Samples of the compounds are available from the authors.

562 © 2019 by the authors. Submitted to *Remote Sens.* for possible open access publication
563 under the terms and conditions of the Creative Commons Attribution (CC BY) license
564 (<http://creativecommons.org/licenses/by/4.0/>).

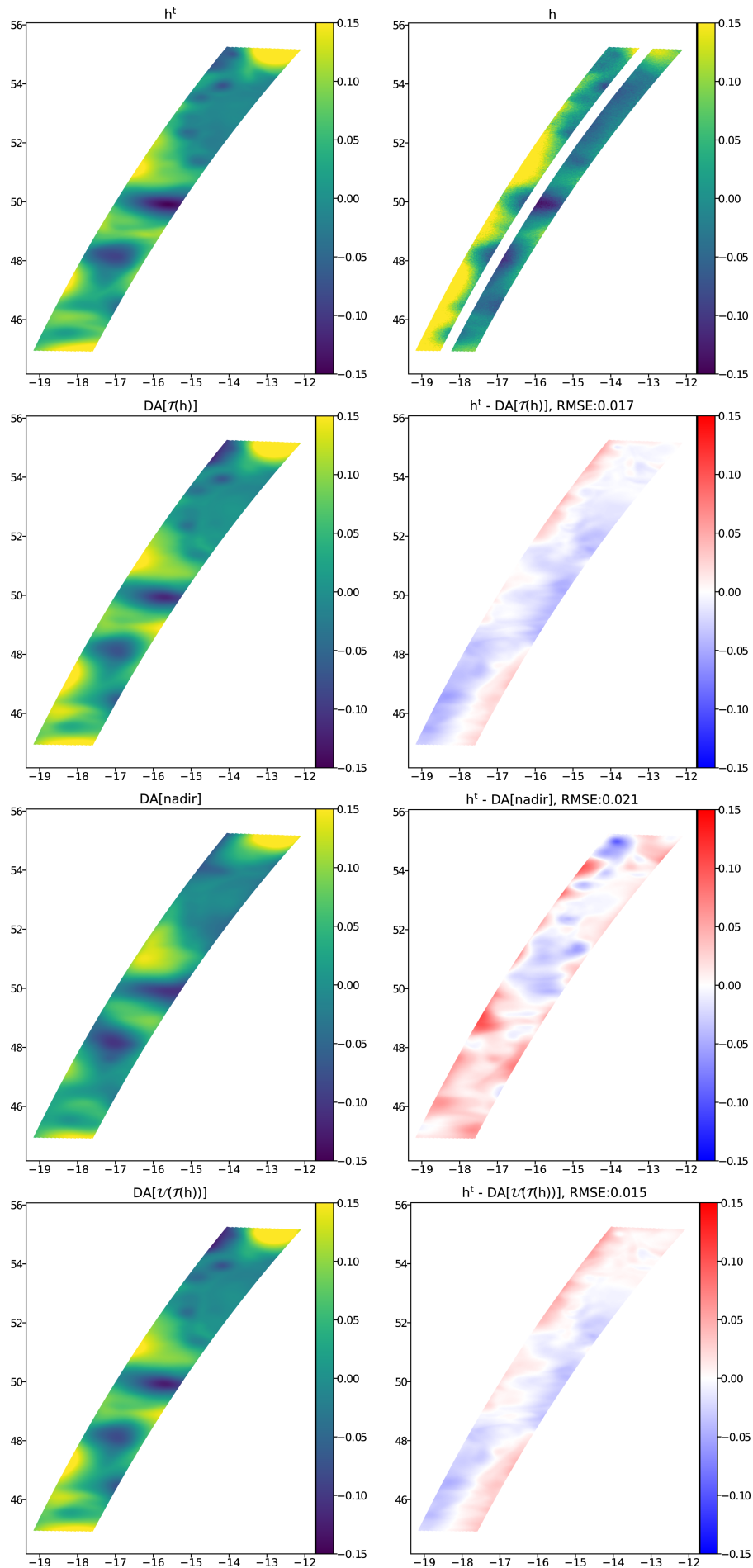


Figure 8. Same as Figure 5 but comparing two additional results: DA[nadir] and DA[$\mathcal{U}(\mathcal{T}(h))$].

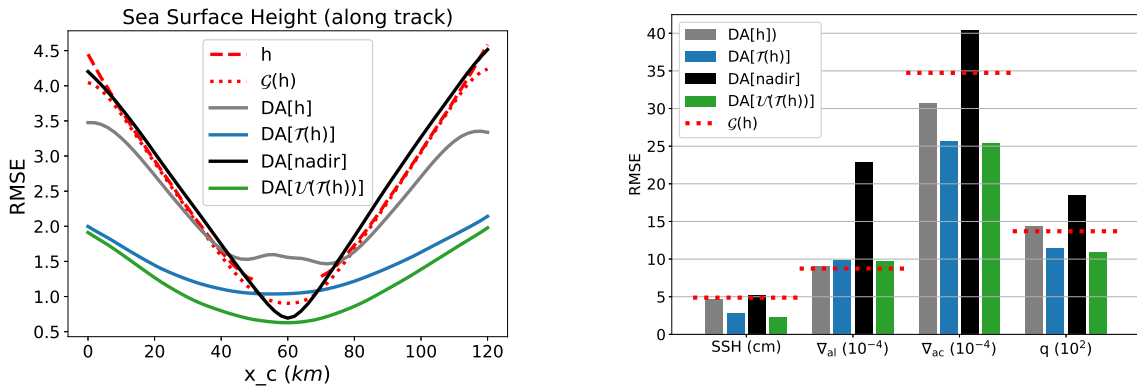


Figure 9. Same as Figure 6 but comparing two additional results: DA[nadir] and DA[$\mathcal{U}(\mathcal{T}(h))$].

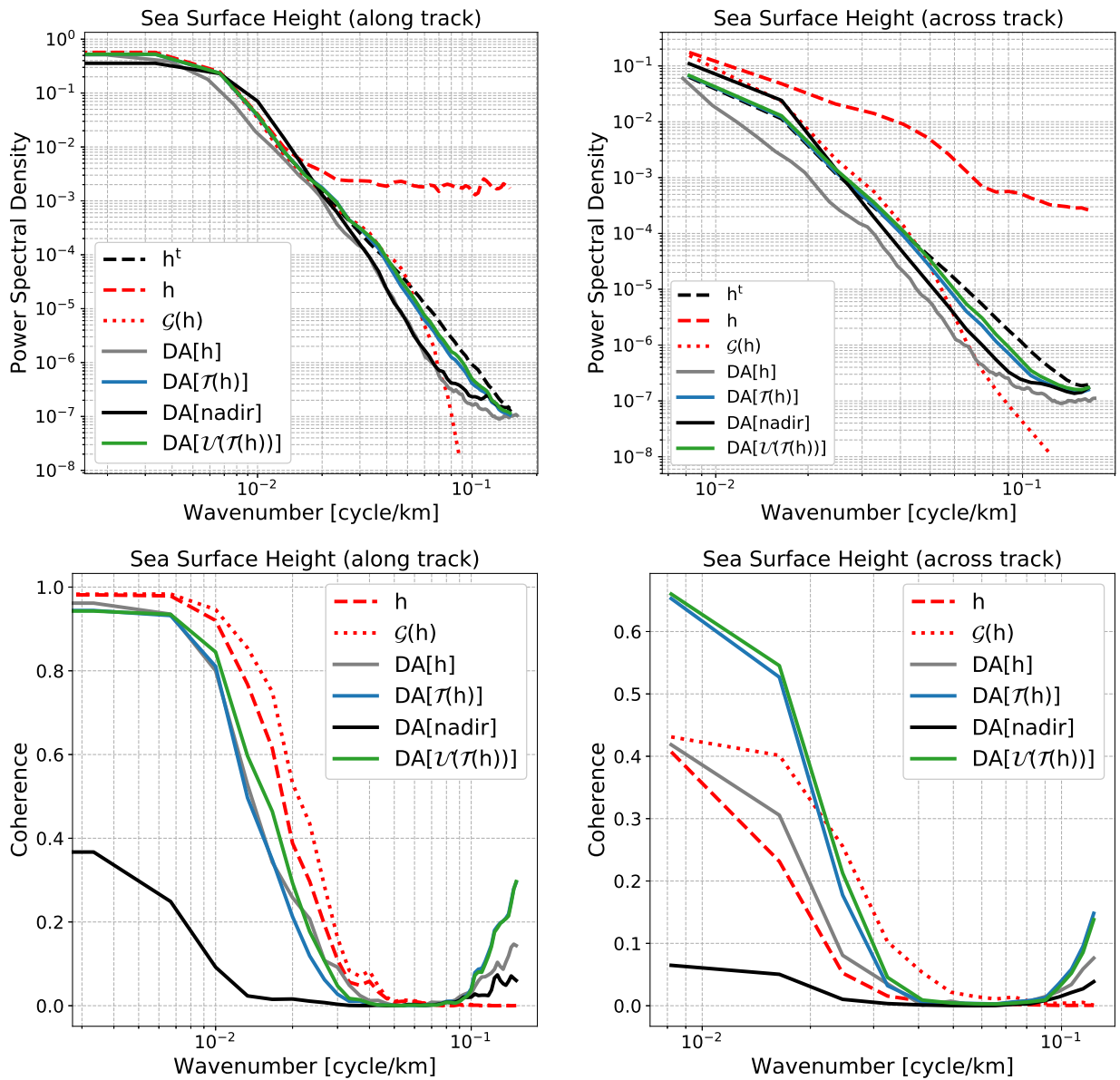


Figure 10. Same as Figure 7 but comparing two additional results: DA[nadir] and DA[$\mathcal{U}(\mathcal{T}(h))$].